ELSEVIER

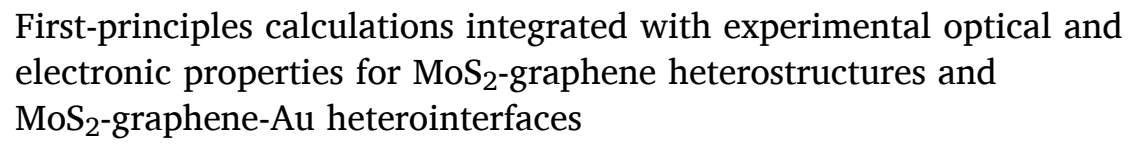
Contents lists available at ScienceDirect

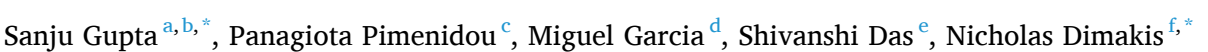
Applied Surface Science

journal homepage: www.elsevier.com/locate/apsusc



Full Length Article





- ^a Department of Materials Science, Penn State University, State College, PA 16801, USA
- ^b Department of Physics, University of Central Florida, Orlando, FL 32816, USA
- ^c Department of Mechanical Engineering, University of West Attica, Athens, Greece
- ^d Mathematics and Science Academy, University of Texas-Rio Grande Valley, Edinburg, TX 78539, USA
- e Allen High School, Allen, TX 75002, USA
- f Department of Physics and Astronomy, University of Texas-Rio Grande Valley, Edinburg, TX 78539, USA

ARTICLE INFO

Keywords: MoS₂/graphene/Au Heterostructures DFT Band structure Work function Dielectric function Reflectivity

ABSTRACT

We present a computational and experimental study for various heterostructures and heterointerfaces comprising two-dimensional (2D) molybdenum disulfide (MoS₂) and graphene (Gr) supported on gold (Au). These structures are useful for photo-electrochemical and nanophotonic applications, as well as for hydrogen generation. The frequency-dependent dielectric function, the refractive index, and the reflectivity are calculated using light polarization parallel and perpendicular to the respective monolayer c axis. We identify the transitions within MoS₂ and graphene, which correspond to peaks in the imaginary part of the frequency-dependent dielectric function. The Gr-MoS₂ dielectric function appears as a composition of the corresponding dielectric functions from the isolated monolayers with their peaks being shifted. However, for the Gr-MoS₂-Au heterointerfaces, some of these peaks from the isolated monolayers are no longer detected. Charge transfers and work function calculations show that MoS₂ and graphene are n and p-type semiconductors, respectively, which agree with our experimental local photoconductivity measurements. The heterojunction behavior for Gr-MoS₂ is attributed to the interlayer electronic coupling, while minimizing Fermi level pinning at the MoS₂/Au interface and charge transfers from graphene to MoS₂. Thus, interfacing MoS₂ with graphene signifies substrate engineering, allowing tunable MoS₂ physical properties for diverse applications across the electromagnetic spectrum.

1. Introduction

The isolation of a single layer graphene from graphite by micromechanical exfoliation and its remarkable properties with demonstrative performance sparked enormous interests in two-dimensional (2D) materials, for both in the fundamental mesoscale physics and in the applied sciences [1–3]. Graphene (Gr) has a zero bandgap (though a very small bandgap opens with substrate interaction), therefore limiting nanoelectronics and photonic applications [1]. Among the van der Waals layered solids, and more specific the 2D transition metal dichalcogenides, molybdenum disulphide (MoS₂) is a promising class of atomic thin semiconductors awaiting its usage in industry applications besides in hydrogen evolution reaction and in photo-electrochemical anodes [4–6]. The thickness dependent transition to direct electronic bandgap ($E_g \sim 1.80~eV$) at the MoS $_2$ monolayer limit (MoS $_2$ -1L) [7], gives rise to strong light absorption resulting in efficient photogenerated electron-hole pairs (known as excitons) coveted for exciton-photon physics and many-body quantum science [8–10]. Thus, the application of new layered materials in nanotechnology opens new perspectives and enables ground-breaking innovations. Moreover, the creation of van der Waals heterostructures (vdWHs) with tunable properties from various combinations of modern 2D materials with clean interfaces is a promising task focused on improving the parameters for nanoscale devices. Furthermore, the semiconductor-metal junction is the most effective for device performance. The large-area and single-crystalline epitaxial growth of 2D transition metal chalcogenides

E-mail addresses: sgup77@gmail.com (S. Gupta), nicholas.dimakis@utrgv.edu (N. Dimakis).



^{*} Corresponding authors at: Department of Materials Science, Penn State University, State College, PA 16801, USA (S. Gupta). Department of Physics and Astronomy, University of Texas-Rio Grande Valley, Edinburg, TX 78539, USA (N. Dimakis).

(TMDs) is one of the most important requirements to meet the challenging demands implied by the semiconductor industry. Therefore, their integration relying on industry-compatible manufacturing processes is still a major challenge, thereby restricting their applications primarily to research laboratories environments.

Recently, the vdWHs are exemplified by experimental demonstration of vertical and lateral heterostructures consisting of graphene (semimetallic), hexagonal boron nitride (dielectric; h-BN), and TMDs (semiconducting) [11-15]. Therefore, it can create an extensive library of vdWHs displaying new physics [16,17] and unique functionality [18], not available in the individual constituents and bulk counterparts. For example, Lopez-Sanchez and co-workers have shown that the TMDs heterostructures are used in photovoltaic and optoelectronic devices because they exhibit very strong light-matter interactions [19]. Other reports include flexible photovoltaics with enhanced external quantum efficiency (~30 %), broadband photodetector with higher responsivity based on Gr/MoS₂(1L)/Gr over a long working wavelength (405 to 2000 nm) [9,20-22], and augmented brightness and reduced contact resistance light emitting diodes constructed from WS₂/Gr [23]. The introduction of graphene offered an ideal platform to unveil 2D semiconductor-2D semimetal heterojunction along with other aspects. Thus, interfacing MoS₂ with graphene, in contrast to similar TMD-based heterostructures, has been proved versatile due to weaker interlayer coupling contributing to marginally improved physical-chemical (electronic, optical, electrochemical, and electrocatalytical) properties [24]. Although, the photonic and electronics properties of Gr/MoS₂ vertical heterostructures have been previously studied [25,26], those reports are focused on nanoelectronic transport mobilities and do not usually discuss the role of graphene in influencing the physicochemical properties. Besides, many theoretical studies have focused on the electronic properties and the formation of the Schottky barrier in the vdW heterostructures [27]. It is conceivable that the physical-chemical properties and applications of the vdWHs depend on the stacking sequence of the constituent layers, the layer number, and the supporting platform.

Computationally, Qiu et. al., [28] reported electronic and optical properties for Gr/MoS₂(1L) heterostructures using density functional theory (DFT) [29,30] calculations and compared them with corresponding calculations from isolated graphene and MoS2 monolayers. The authors reported that a minigap appears at the graphene Dirac point of the Gr/MoS₂, in agreement with other reports [31,32]. Moreover, they also reported that the absorption coefficient, refractive index, and the reflectance are redshifted in the heterostructure. The electronic properties of MoS₂(1L)/Au (111) have been reported by Bruix et al. using angle-resolved photoemission spectroscopy, scanning tunneling spectroscopy, and DFT [33]. The authors found that the MoS₂(1L) bandgap of MoS₂/Au (111) is the same to those of the freestanding monolayer MoS₂. Yortanli and Mete reported Gr/Au (111) electronic calculations, where they found a downward shift of the Fermi energy (E_{Fermi}) with respect to graphene's Dirac point showing a p-type doping character [34]. However, we are not aware of a computational study of $MoS_2(1L)/Gr/Au$ heterointerfaces.

In the present work, we consider the electronic and optical properties of the MoS_2 layers and their heterostructures with graphene and gold heterointerfaces using DFT for calculating band structure, electronic density of states, surface work function, and resulting charge transfers at various interfaces. The frequency-dependent dielectric functions and reflectivity spectra are calculated in a large wavelength window useful for optoelectronics, quantum optics, and single-photon emitters for telecommunication. The real and imaginary parts of the dielectric function are related to the refractive index and the absorption coefficient, respectively. While the monolayer MoS_2 is a direct semiconductor, and graphene is gapless, the MoS_2 /Gr heterostructure still reveals a direct bandgap somewhat than that of the monolayer MoS_2 . In the heterostructures, while the contribution of Mo-d orbitals to the conduction band is outstanding, the Mo-p, Mo-d, and C-p orbitals contribute

to the valence band. The relocation and rehybridization of the orbital in the monolayer MoS_2 to form a heterostructure with graphene brought interesting properties that can be applied in the phototransistors based on MoS_2/Gr heterostructures. The computational findings are correlated with experimental optical (photoluminescence spectroscopy), vibrational properties (Raman spectroscopy), and work function from Kelvin probe force microscopy (KPFM) elucidating the effect graphene layer has on $MoS_2(1L)$ properties.

2. Experimental

2.1. Materials and methods

The experimental methods and measurements carried out are described briefly here, (see ref. [35] for details). We fabricated vertical heterostructures comprising of $MoS_2(1L)$ and graphene using an efficient dry transfer method on freshly prepared gold Au (111) coated SiO_2/Si substrates imaged using electron microscopy (SEM) and atomic force microscopy (AFM). We investigated optical (UV–Visible absorption, photoluminescence-PL, and Raman spectroscopy) and electronic (work function and photoconductivity) properties to explore various surfaces and heterointerfaces to signify the interaction with Au substrate and graphene layer, the latter interspersed as 'nanospacer' to minimize PL quenching due to underneath gold and enhance photoconduction for optoelectronic properties and energy harvesting applications.

2.2. Computational calculations of electronic and optical properties unit cell modeling

The isolated monolayers $2H\text{-}MoS_2$ ($MoS_2\text{-}1L$) and graphene (Gr) were generated as 4×4 $P6_3/mmc$ supercell lattices, with lattice constants 12.76 Å and 9.87 Å, respectively. The isolated $MoS_2(1L)$ supercell is three-layered totaling 48 atoms, with 32 S atoms occupying the top and bottom layers and 16 Mo atoms residing in the middle layer. The isolated graphene supercell has 32 atoms. Four-layer Au supercells, at the $(1\,1\,1)$ crystallographic phase, were used. The Gr/MoS_2 and $MoS_2/Gr/MoS_2$ heterostructures supercells were selected as 4×4 and 5×5 supercells for MoS_2 and graphene, respectively, such that the lattice mismatch is small. Similar selection of supercells is used for the remaining structures of this work. Figs. 1 and 2 show the DFT optimized unit cells and the electronic structure for Gr/MoS_2 , $Gr/MoS_2(1L)/Gr$, for Gr/Au, and for $MoS_2(1L)/Au$, $MoS_2(2L)/Au$, and $MoS_2(1L)/Gr/Au$, respectively.

Simulations Design and Data Analysis: We performed DFT electronic structure calculations for the optimal geometries of various MoS₂graphene heterostructures and corresponding heterointerfaces with Au (111) using the periodic code Vienna Ab initio Simulation Package (VASP) [36-39]. The projector augmented-wave (PAW) pseudopotentials were used [40,41]. The Kohn-Sham equations were solved using the generalized gradient approximation (GGA) under the Perdew-Burke-Ernzerhof (PBE) functional [42]. We used the D3 semiempirical correction by Grimme [43], which improves the DFT functionals descriptions for the long-range electron correlations responsible for van der Waals interactions. The kinetic energy cutoff for all calculations is 600 eV, thus ensuring the integrity of our results. The electronic band structures are plotted including the per atom and corresponding (s, p, d) orbital contributions. The convergence criteria for energy self-consistent field (SCF) and geometry optimizations were set at $10^{\text{-}9}\,\text{eV}$ and $10^{\text{-}4}\,\text{eV/Å}$ per atom, respectively. The Brillouin-zone (BZ) was sampled using the $\Gamma\text{-centered}$ $6\times6\times1$ BZ grid for all calculations in this work. For the isolated graphene, the denser $9 \times 9 \times 1$ grid was also used. The work function Φ was obtained from the equation:

$$\Phi = E_{vaccum} - E_{Fermi} \tag{1}$$

where E_{vaccum} is obtained from the planar average potential

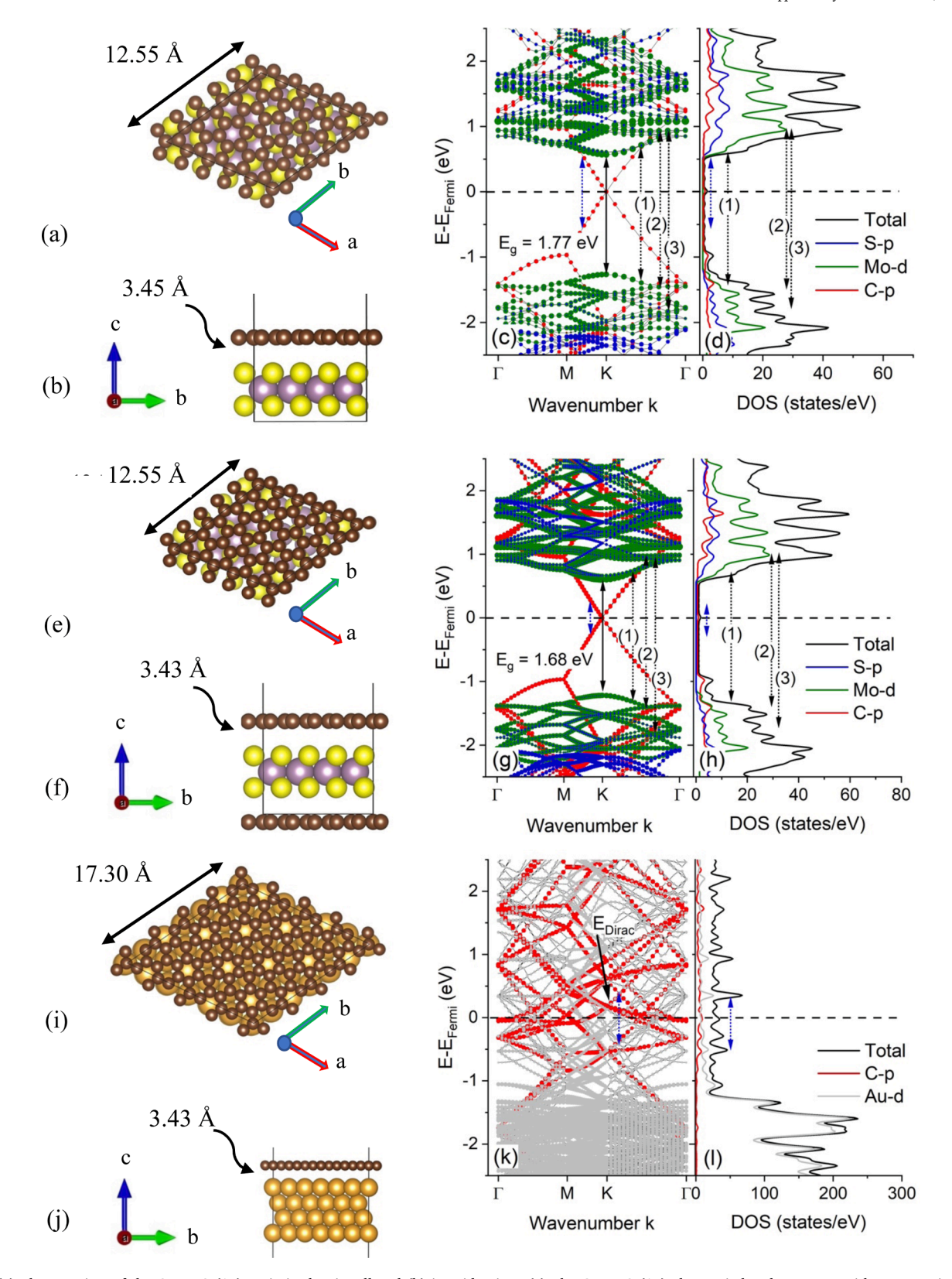


Fig. 1. (a) The top view of the $Gr/MoS_2(1L)$ optimized unit cell and (b) it's side view. (c) The $Gr/MoS_2(1L)$ electronic band structure with atom projections and corresponding total and (d) its projected DOS per atomic orbital. (e) The top view of the $Gr/MoS_2(1L)/Gr$ optimized unit cell and (f) its side view. (g) The $Gr/MoS_2(1L)/Gr$ electronic band structure with atom projections and corresponding total and (h) its projected DOS per atomic orbital. (i) The top view of the $Gr/MoS_2(1L)/Gr$ optimized unit cell and (j) its side view. (k) The $Gr/MoS_2(1L)/Gr$ electronic band structure with atom projections and corresponding total and (l) its projected DOS per atomic orbital. *In optimized geometries*: Atoms are colored as follows: Mo, purple; S, yellow; Au, orange; C; brown. The thin lines denote the unit cell boundaries. *In electronic band structure*: The dashed horizontal line is the Fermi energy (E_{Fermi}). The solid double arrows show the MoS_2 bandgaps (E_g). The black and blue dotted double arrows show transitions within the MoS_2 and the graphene $\pi \rightarrow \pi^*$ transitions, respectively. (For interpretation of the references to colour in this figure legend, the reader is referred to the web version of this article.)

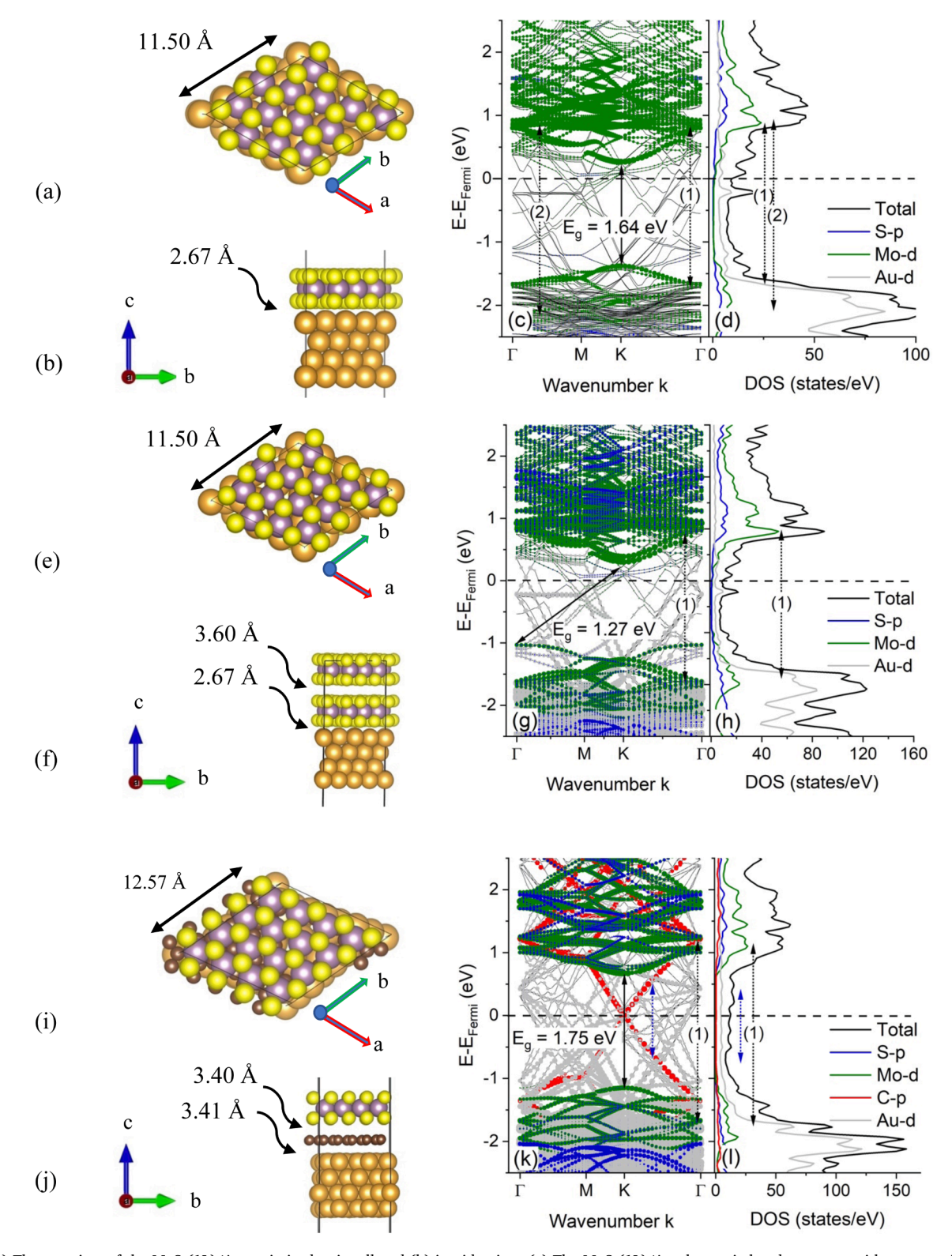


Fig. 2. (a) The top view of the $MoS_2(1L)/Au$ optimized unit cell and (b) its side view. (c) The $MoS_2(1L)/Au$ electronic band structure with atom projections and corresponding total and (d) its projected DOS per atomic orbital. (e) The top view of the $MoS_2(2L)/Au$ optimized unit cell and (f) its side view. (g) The $MoS_2(2L)/Au$ electronic band structure with atom projections and corresponding total and (h) its projected DOS per atomic orbital. (i) The top view of the $MoS_2(1L)/Gr/Au$ optimized unit cell and (j) it's side view. (k) The $MoS_2(1L)/Gr/Au$ electronic band structure with atom projections and corresponding total and (l) its projected DOS per atomic orbital. In optimized geometries: Atoms are colored as follows: Mo, purple; S, yellow; Au, orange; C; brown. The thin lines denote the unit cell boundaries. In electronic band structure: The dashed horizontal line is the Fermi energy (E_{Fermi}). The solid double arrows show the MoS_2 bandgaps (E_g). The black and blue dotted double arrows show transitions with the MoS_2 and graphene $\pi \rightarrow \pi^*$ transitions, respectively. (For interpretation of the references to colour in this figure legend, the reader is referred to the web version of this article.)

calculations.

Bader-type ion charges [44] were obtained using the Bader Charge Analysis code by Henkelman and co-workers [45–48], which partitions the charge density grid into Bader-type volumes. This code scales linearly with the number of grid points and can be used by large unit cells.

2.3. Mathematical formalism of optical properties

Since the substrate and the interface with other 2D materials in 2D- MoS_2 strongly affects the physical properties, it is natural to expect that it also provides vital effects on the optical properties. To study the optical properties computationally, we use the frequency-dependent dielectric function written as:

$$\varepsilon(\omega) = \varepsilon_R(\omega) + i\varepsilon_I(\omega) \tag{2}$$

where $\varepsilon_R(\omega)$ and $\varepsilon_I(\omega)$ are the real and imaginary parts of dielectric function, respectively, and ω being the photon energy. The imaginary part $\varepsilon_I(\omega)$ can be obtained computationally from the summation over the occupied and unoccupied states following the equation [49,50]:

$$\varepsilon_{I}^{i,j}(\omega) = \frac{4\pi^{2}e^{2}}{Vm^{2}\omega^{2}} \sum_{c,v} \int_{BZ} dk \langle U_{ck}|p_{i}|U_{vk}\rangle \langle U_{ck}|p_{j}|U_{vk}\rangle \delta(\omega_{ck}(k) - \omega_{vk}(k) - \omega)$$
(3)

where e and m are the electron charge and mass, respectively, V is the unit cell volume, p is the momentum operator, c and v are the conduction and vallence bands, respectively, U_{ck} is the the crystal wave function, which corresponds to energy E_{ck} , and j = x, y, z. The real part is calculated from the imaginary part via Kramers-Kronig relation:

$$\varepsilon_R(\omega) = 1 + \frac{2}{\pi} \int_1^{\omega} \frac{\omega_1 \varepsilon_I(\omega_1) d\omega_1}{\omega_1^2 - \omega^2}.$$
 (4)

For compounds having hexagonal symmetry as opposed to cubic symmetry, the dielectric properties are performed with electric field parallel and perpendicular to the crystallographic c-axis [51]. Thus, the measured dielectric functions are denoted by $\varepsilon_{(R,I)}^{E\parallel c}$ and $\varepsilon_{(R,I)}^{E\perp c}$ and given by [51]:

$$\varepsilon^{E\perp c}(\omega) = \frac{1}{2} \left[\varepsilon^{xx}(\omega) + \varepsilon^{yy}(\omega) \right], \tag{5}$$

$$\varepsilon^{E||c}(\omega) = \varepsilon^{zz}(\omega)$$
 (6)

The corresponding refractive index $n(\omega)$, the extinction coefficient $k(\omega)$, and the reflectivity $R(\omega)$ are given in terms of $\varepsilon_R(\omega)$, $\varepsilon_I(\omega)$, $n(\omega)$, and $k(\omega)$ following:

$$n(\omega) = \frac{1}{\sqrt{2}} \left(\sqrt{\left[\varepsilon_R(\omega)^2 + \varepsilon_I(\omega)^2\right]^{\frac{1}{2}}} + \varepsilon_R(\omega) \right)^{\frac{1}{2}}$$
 (7)

$$k(\omega) = \frac{1}{\sqrt{2}} \left(\sqrt{\left[\varepsilon_R(\omega)^2 + \varepsilon_I(\omega)^2 \right]^{\frac{1}{2}}} - \varepsilon_R(\omega) \right)^{\frac{1}{2}}$$
 (8)

or
$$\alpha(\omega) = \frac{\sqrt{2}}{c}\omega(\sqrt{\left[\varepsilon_R(\omega)^2 + \varepsilon_I(\omega)^2\right]^{\frac{1}{2}}} - \varepsilon_R(\omega))^{\frac{1}{2}}$$
, (8').

$$R(\omega) = \left| \frac{\sqrt{\varepsilon_I(\omega) + \varepsilon_R(\omega)} - 1}{\sqrt{\varepsilon_I(\omega) + \varepsilon_R(\omega)} + 1} \right|^2 = \frac{(n(\omega) - 1)^2 + k(\omega)^2}{(n(\omega) + 1)^2 + k(\omega)^2}$$
(9)

The optical properties are calculated using the independent particle approximation (IPA) [52]. We also used the random phase approximation (RPA) [53] for graphene to check the accuracy of the IPA method. In general, RPA is superior to IPA. However, even for isolated graphene, RPA optical properties calculations requires huge RAM (>10 Tb) and thus it is impractical for being used by large supercells. All the calculations were run on the Texas Advanced Computer Center (TACC) supercomputer facilities, using the Stampede 2 and Lonestar 6 supercomputers.

3. Results and discussion

3.1. DFT calculated electronic structure and optical properties

Here, we discuss the electronic and optical properties of mono and bilayer MoS_2 coupled with graphene and gold calculated using DFT for the optimized structures shown in Figs. 1 and 2. This study specifically focuses on the band structure, the density of states, the work function, the charge transfer, the frequency-dependent dielectric function, the refractive index, and the reflectivity.

Isolated graphene. The DFT calculated dielectric functions for the isolated graphene and the MoS2 have been reported [54-60]. Here, we have also calculated the dielectric function ε , the refractive index n, and the reflectivity R for the above-mentioned optimized geometries using the IPA (Fig. S1, Supplementary Materials). The use of a denser BZ grid reveals several peaks in the energy region 0 - 5 eV, for the in-plane polarization component of the imaginary part of graphene's dielectric function $\varepsilon_{\rm I}^{{\rm E}\perp c}$. Marinopoulos et. al., have assigned these peaks to the interband $\pi \rightarrow \pi^*$ transitions, whereas the peaks between 11.67 - 19.91 eV corresponds to the $\sigma \rightarrow \sigma^*$ transitions [55]. Increased BZ grid minimally affects the peaks, which correspond to the $\sigma \rightarrow \sigma^*$ transitions. Similarly, for the IPA calculations, the out of plane polarization $\varepsilon_{\rm L}^{E//c}$ component shows peaks at 10.92 eV and 14.47 eV, which correspond to the interband $\pi \rightarrow \sigma^*$ and $\sigma \rightarrow \pi^*$ transitions, respectively [59]. Our isolated graphene in plane component of the dielectric constant (i.e., $\varepsilon_R^{E\perp c}(0))$ is 5.63 and 7.46 for the IPA calculations under the $6\times 6\times 1$ and 9 \times 9 \times 1 BZ grids, respectively. The corresponding out of plane component $\varepsilon_p^{E//c}(0)$ has a lower value of 1.56 for both type of grids. Our dielectric constant values comply with Rani et. al., who reported dielectric constant values of 7.6 and 1.25 for the in plane and out of plane components, respectively. Table 1 shows the energy locations from the $\varepsilon_I(\omega)$ spectrum for the most prominent transitions of graphene and MoS2 for all systems studied in this work.

The imaginary part of the dielectric function (ε_I) for the isolated graphene has been also calculated using the random phase approximation (RPA) under the $6\times 6\times 1$ BZ grid. The RPA includes crystalline local effects. These RPA calculations were performed using a coarser grid for the representation of the pseudo-orbitals, which is about half the size used in all other calculations (Fig. S2, Supplementary Materials). This is due to the RPA's high memory requirements. Fig. S2 shows an excellent agreement between IPA and RPA calculated ε_I for the in-plane polarization component (i.e., $\varepsilon_I^{E\perp c}$). However, there are differences in the out of plane amplitudes $\varepsilon_I^{E//c}$ between these IPA and RPA calculations. This is in agreement with a past report, which emphasizes the role of local effects in the out of plane calculations [55]. The RPA and IPA calculations using the coarser grid for the representation of the pseudo-orbitals show a continuum spectrum for the in-plane polarization $\varepsilon_I^{E\perp c}$, in agreement with past reports [54,59].

Isolated MoS₂ monolayer. The imaginary part of dielectric function for the isolated MoS₂ monolayer (MoS₂-1L) shows peaks maxima at 2.89 eV and 5.48 eV, for in plane and out of plane components, respectively (Fig. S3a-S3b, Supplementary Materials). The $\varepsilon_1^{E\perp c}(\omega)$ appears redshifted relative to $\varepsilon_1^{E//c}(\omega)$, in agreement with past work [28,61–63]. However, there are cases, that these spectra have been reported in a reverse order [57,64]. As it will be explained below, the MoS₂(1L) maxima peaks from $\varepsilon_1^{E\perp c}(\omega)$ and $\varepsilon_1^{E//c}(\omega)$ also appear in the Gr-MoS₂ heterostructures, thus verifying the correctness of our approach. Figs. 1 and 2 show the optimized unit cells, their band structures, and the densities of states (DOS) for all heterostructures and heterointerfaces examined here. The $\varepsilon_1^{E\perp c}(\omega)$ and $\varepsilon_1^{E//c}(\omega)$ peaks for the isolated MoS₂(1L) correspond to the transitions namely, Mo_{dxy,x^2-y^2} , $S_{p_z} \rightarrow Mo_{dxy,x^2-y^2}$ and Mo_{dxz,zy,z^2} , $S_{p_x} \rightarrow Mo_{dxz,zy,z^2}$, respectively [58]. Our calculated MoS₂ (1L) bandgap is 1.61 eV, which is close to the experimental value of 1.80 eV [4]. The

Table 1
The peak positions for the imaginary part of the dielectric function and the corresponding transitions for graphene and MoS₂. The valance and the conduction band for MoS₂ are as follows: $V_{E \perp c} = Mo_{dxy,x^2-y^2}, S_{p_z}$ $C_{E \perp c} = Mo_{dxy,x^2-y^2}, V_{E//c} = Mo_{dxx,xy,z^2}, S_{p_xy},$ and $C_{E//c} = Mo_{dxx,xy,z^2}$. Values in square brackets are for the IPA calculations under the 9 × 9 × 1 BZ grid, whereas values in regular brackets refer to RPA calculations.

System	Graphene		MoS ₂			
	$\pi \rightarrow \pi^*$	$\sigma{ ightarrow}\sigma^*$	$\pi{ ightarrow}\sigma^*$	$\sigma{ ightarrow}\pi^{^{*}}$	$V_{\rm E\perp c} \rightarrow C_{\rm E\perp c}$	$V_{\rm E//c} \rightarrow C_{\rm E//c}$
	(eV)					
Gr	1.36-3.82	11.67-19.91	10.92	14.47		
	[0.90-4.00]	[11.67–19.21]	(12.18)	(15.15)		
	4.00^1 ; 4.6^2	13.8^{1} ; 14.00^{3}	12.00^3	14.5^{3}		
MoS_2 (1L)					1.79; 2.07; 2.86	3.67; 5.46
					1.70^4 ; 3.39^4 ; 2.80^4	3.71; 5.56
Gr/MoS ₂ (1L)/Gr	0.49; 1.27; 3.78	11.17–16.34	11.39	14.15	2.06; 2.32; 2.79	3.71; 5.47
Gr/MoS ₂ (1L)	1.04; 1.56; 3.76	11.14–18.67	12.18	14.09	1.98; 2.28; 2.78	3.71; 5.55
MoS ₂ (2L)/Au					2.78	5.43
MoS_2 (1L)/Au					2.45; 2.91	5.47
Gr/Au	0.68-2.39	not resolved	11.56	14.20		
MoS ₂ (1L)/Gr/Au	0.99-2.78	not resolved	not resolved	14.05	2.85	5.50

Note: ¹RPA calculated value [59]; ²Experimental value [54]; ³RPA calculated values [54]. ⁴DFT values from [58].

high dielectric constant $\varepsilon_R(0)$ out of plane component indicates that $\text{MoS}_2(1\text{L})$ is suitable for solar cell applications [65], whereas the out of plane high refractive index of 3.73 at around 2.6 eV shows that $\text{MoS}_2(1\text{L})$ can also serve as antireflection coating for flat panel displays. The $\text{MoS}_2(1\text{L})$ high reflectivity shows that it is a good reflector from IR to UV (i.e., in a wider electromagnetic spectral window). The high value of the MoS_2 refractive index in the visible (\sim 2.0 – 2.75 eV) make it suitable to serve as a heat preservation material. It is also noteworthy that such details on the optical properties are challenging to capture experimentally for all heterointerfaces examined here.

Gr/MoS2 and Gr/MoS2/Gr heterostructures. The electronic band structure calculations for the heterostructures Gr/MoS₂(1L), Gr/ MoS₂(1L)/Gr, and the heterointerface MoS₂(1L)/Gr/Au show the presence of the Dirac point at the Fermi energy (EFermi), located at the K point (Figs. 1-2, left panels). Interestingly for the Gr/Au case, the Dirac point is upshifted by about 0.17 eV, which is in an excellent agreement with the past report of Khomyakov et. al., [66] and indicative of physisorption of graphene on Au substrate. A small bandgap of the order of a few meV (minigap) is opened at the Dirac point for all graphene heterostructures in this work, as anticipated when monolayer graphene is placed on substrates. The presence of this minigap has also been reported previously for the $Gr/MoS_2(1L)$ heterointerface [31,32]. The MoS₂(1L) bandgap is in the range of 1.27–1.77 eV (Figs. 1-2), which is close to the value for the isolated MoS₂(1L) bandgap of 1.61 eV found here. While for more than one layer of MoS₂(2L)/Au, the bandgap becomes indirect, as in the MoS₂ bulk case [67].

We examine the changes in the optical properties for the isolated graphene and the MoS₂(1L) due to their presence in the Gr/MoS₂(1L) and Gr/MoS₂(1L)/Gr heterostructures. Fig. 3 shows the frequencydependent optical properties ε , n, and R for all heterostructures and heterointerfaces of this work. The imaginary part of the dielectric function ε_I for the Gr/MoS₂(1L) and Gr/MoS₂(1L)/Gr heterostructures show peaks that correspond to transitions from graphene and MoS2. Table 1 shows that the locations of these peaks in both heterostructures are located at about the same energies to those from isolated monolayers, for both the in plane and out of plane light polarizations. Moreover, all graphene allowed transitions from the π and σ bands towards the π^* and σ^* bands are detected computationally in the ε_I spectra, for both Gr/MoS₂(1L) and Gr/MoS₂(1L)/Gr heterostructures. However, this is not the case for the MoS₂(1L)/Gr/Au heterointerface, as it will be discussed later in this section. The peaks of these transitions appear at about the same positions as the ones from isolated graphene, in a similar fashion as the peaks that correspond to transitions involving MoS₂. This implies that the overlap between graphene and MoS₂(1L) bands is rather small.

The larger values of dielectric constants for the heterostructures

relative to the isolated monolayers manifests that they are better dielectrics than those of isolated MoS_2 and graphene. However, the inplane component of the dielectric constant for the Gr/MoS_2 is smaller than from $Gr/MoS_2(1L)/Gr$, whereas the opposite is observed for the out of plane polarization. The heterostructures refractive index spectra are redshifted relative to the one for the isolated monolayers. This agrees with the past report by Qiu et al., on the DFT calculated optical properties for Gr/MoS_2 [28], as well as with our experimental optical absorption and photoluminescence properties (Figs. 4-5). Moreover, in the visible region, the Gr/MoS_2 has a higher refractive index value relative to the isolated $MoS_2(1L)$, whereas the opposite is observed for the $Gr/MoS_2(1L)/Gr$ configuration. These results agree with those reported by Qiu et al. [28]. Therefore, the Gr/MoS_2 is an improved material for heat preservation applications relative to the isolated MoS_2 (1L).

The reflectivity of the Gr/MoS₂(1L)/Gr is smaller than for Gr/MoS₂(1L) energies up to about 11 eV for both the in plane and out of plane components. An exception to the above statement is observed for the in-plane reflectivity at energies less than 0.6 eV, where we found the following order: $R^{\rm Gr/MoS_2(1L)} < R^{\rm Gr/MoS_2(1L)/Gr}$. The Gr/MoS₂(1L) heterostructure will reflect light better in a wide optical region, since it's out of plane reflectivity is larger as compared with those found for the isolated graphene and MoS₂.

MoS₂(1L-2L)/Au heterointerfaces. The $\varepsilon_{\rm L}^{E\perp c}(\omega)$ component for the MoS₂(1L-2L)/Au heterointerfaces shows peaks at about 1.52 eV, which are absent from the corresponding spectra for the isolated MoS2 monolayer. Johnson and Christy reported the dielectric function for Cu, Ag, and Au through reflection and transition measurements at room temperature [68]. The authors reported that the Au dielectric function imaginary part shows a curve that peaks at about 1.0 eV. In our case, the $\varepsilon_{\rm L}^{E \perp c}$ associated with Au intraband transition from the Au valance bands to the Au-Mo conduction bands peak occurs at about 1.57 eV. For MoS₂(1L)/Gr/Au and Gr/Au, two peaks appear at 1.2 eV and 2 eV, which are associated with the Au intraband transitions, which involve graphene bands. There are significant differences in the real part of the dielectric function $\varepsilon_R(\omega)$ between the MoS₂(1L)/Au and the MoS₂(2L)/ Au, where the MoS2(1L)/Au $\varepsilon_R^{E//c}$ spectrum is comparable to the one from the isolated $MoS_2(1L)$. The dielectric constant for the $MoS_2(2L)/Au$ is significantly higher than the MoS2(1L)/Au, which implies that an additional MoS2 layer on top of MoS2(1L)/Au improves the heterostructure's dielectric properties, as expected. However, both heterointerfaces have similar refractive index n and reflectivity R values, for energies up to about 6 eV. The out of plane component of the refractive index n for the $MoS_2(1L-2L)/Au$ heterointerfaces is significantly larger than the corresponding value for the isolated MoS₂(1L) and for the Gr-MoS₂ heterostructures examined above, for energies up to about 1.6 eV,

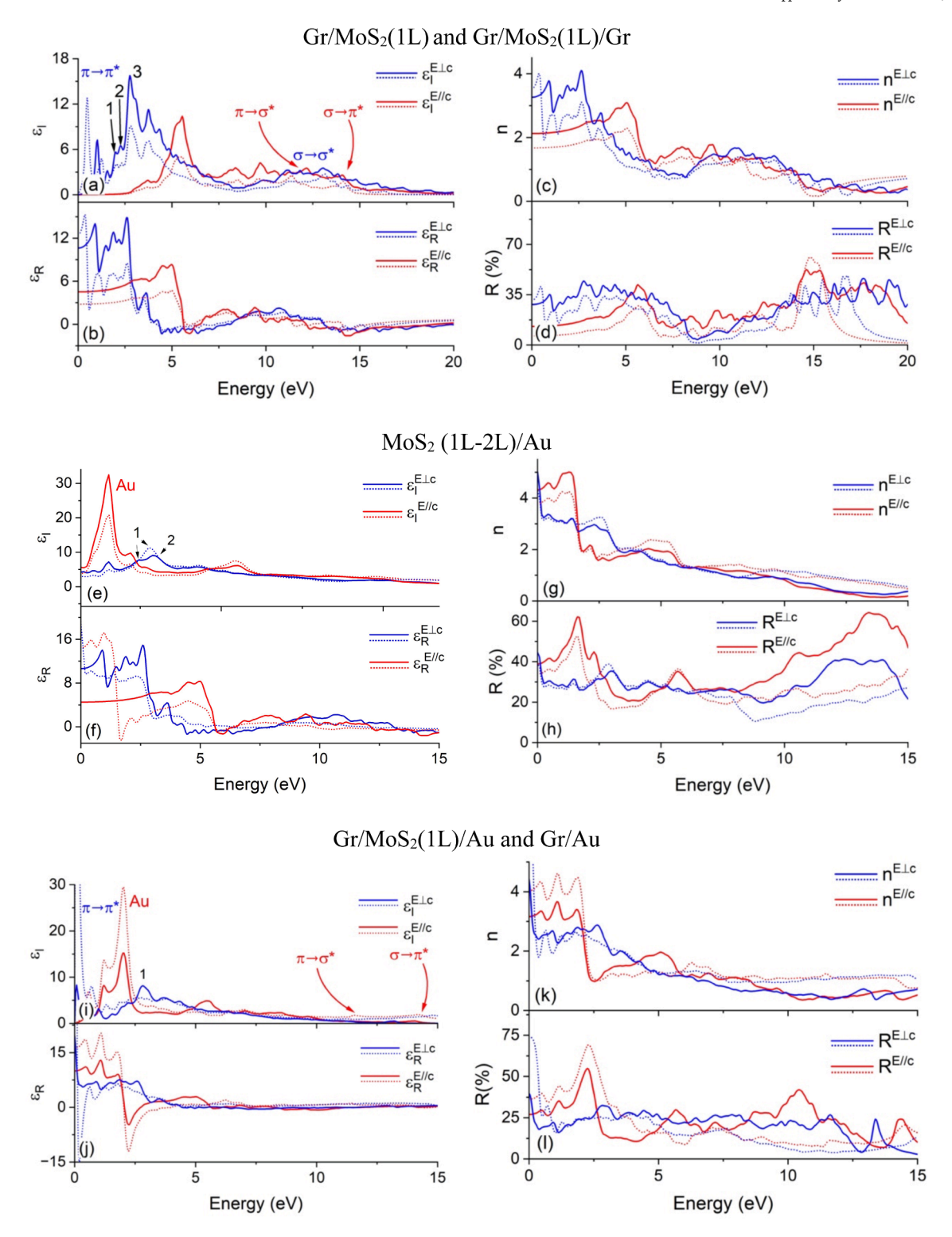


Fig. 3. (a) The imaginary part of dielectric functions $ε_l$ for Gr/MoS₂ (solid lines) and Gr/MoS₂(1L)/Gr (dotted lines), (b) the real part $ε_R$, (c) the refractive indices n, and (d) reflectivity R, (e) the $ε_l$ for MoS₂(1L)/Au (solid lines) and MoS₂(2L)/Au (dotted lines), (f) their $ε_R$, (g) n, and (h) R. (i) The $ε_l$ for Gr/MoS₂/Au (solid lines) and Gr/Au (dotted lines), (j) their $ε_R$, (k) n, and (l) R. The parallel (//) and the perpendicular (\bot) components are shown. The numbers in the $ε_l$ peaks are related to transitions within the MoS₂ from its valence band to its conduction band, as shown in Figs. 1 and 2. The label Au refers to transitions that involve Au bands predominantly.

with $n^{\text{MoS}_2(1L)/\text{Au}} > n^{\text{MoS}_2(2L)/\text{Au}}$, with the $\text{MoS}_2(1L)/\text{Au}$ $n^{E//c}$ being the highest for all configurations of this work. This makes the $\text{MoS}_2(1L-2)/\text{Au}$ and Gr/Au materials useful for thermal (IR) coatings.

MoS₂(1L)/Gr/Au and Gr/Au heterointerfaces. It was experimentally observed that freshly prepared gold coated Si substrate, used for

investigating the exfoliated graphene and MoS₂, influences their physical properties (Figs. 4-5) [7,35,69,70]. Here, we investigated computationally how Au influenced graphene optical properties for the MoS₂(1L)/Gr/Au and the Gr/Au heterointerfaces. Specifically, the $\varepsilon_1^{\rm E\perp c}(\omega)$ for the MoS₂(1L)/Gr/Au and Gr/Au shows several peaks in the

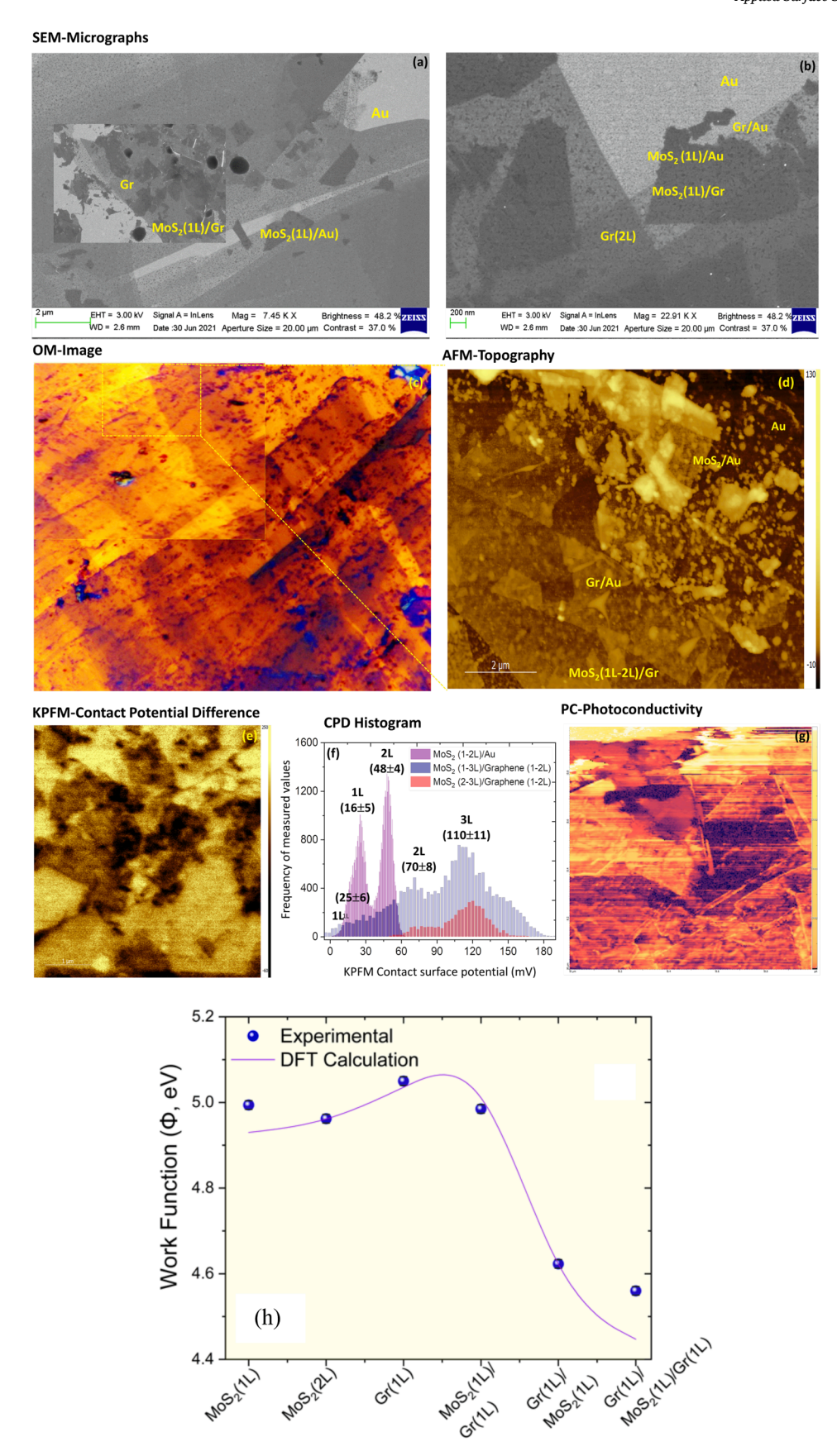


Fig. 4. (a, b) SEM microscopy images in two magnifications showing graphene and MoS_2 surfaces and interfaces contrast (c) Optical microscopy image (d) AFM image revealing surface topography. Corresponding (e) contact potential difference (CPD) measured using KPFM, (f) CPD distribution of MoS_2 /Au and MoS_2 /graphene interfaces, (g) photoconductivity maps, and (h) Variation of work function values.

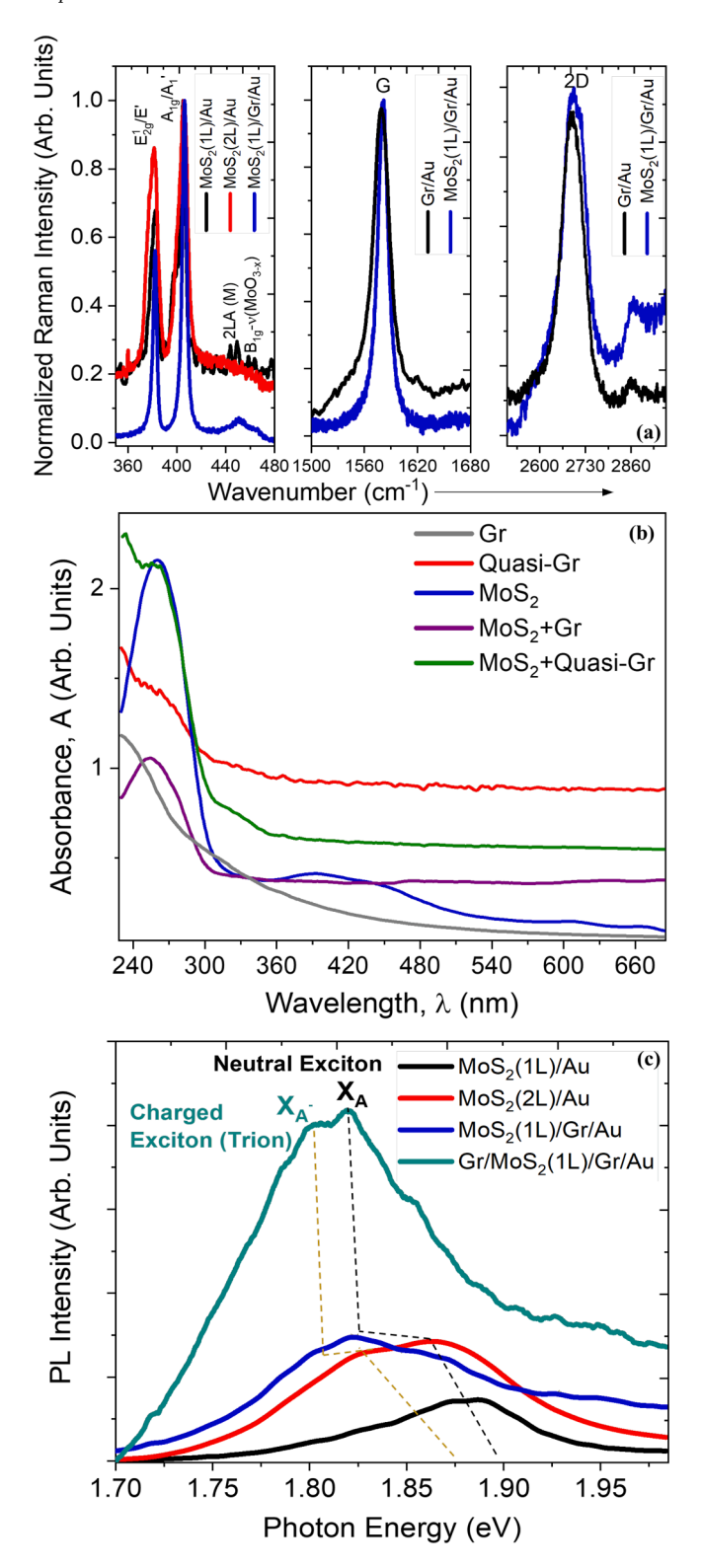


Fig. 5. (a) Confocal Raman spectra measured using 633 nm excitation showing prominent bands associated with MoS $_2$ (E_{2g}^1 , A_{1g}), graphene (G, 2D) and heterointerfaces. (b) UV–Vis optical absorption spectra of graphene, quasigraphene, MoS $_2$ and mix of graphene and MoS $_2$ showing characteristic graphene and MoS $_2$ bands. (c) Room temperature photoluminescence (PL) spectra showing neutral exciton (A) and charged exciton-trion (A) peaks. The dashed line is drawn to guide eye.

energy range 0.99 - 2.68 eV and 0.69 - 2.39 eV, respectively, which correspond to the $\pi\to\pi^*$ transitions. However, the $\sigma\to\sigma^*$ transitions cannot be identified from heterointerfaces $\epsilon_1^{E\perp c}(\omega)$ spectra. The intense peaks at about 1.2 eV and 2 eV in the $\epsilon_1^{E//c}(\omega)$, which involve transitions within the Au bands mixed with graphene bands for the MoS2(1L)/Gr/Au case, are corroborated with experimental observations reflected in the changes in the optical emission peaks through redshifts, as well as in the vibrational bands due to stronger electron–phonon coupling (vide infra). The MoS2(1L)/Gr/Au has the highest dielectric constant from all materials examined here, which makes MoS2(1L)/Gr/Au a suitable material candidate for photovoltaic solar cell applications. The out of plane component of the reflectivity for the Gr/Au heterointerface showed its highest value at about 2.25 eV from all structures of this work.

Charge transfer and work function. Table 2 summarizes the charges per Mo, S, C, and Au relative to their isolated atoms charges and the work function for all configurations studied in this work. In all configurations, there is some small electron transfer per atom from graphene to Au and MoS_2 , which makes graphene is a p-type semiconductor in the heterostructures and heterointerfaces. Similarly, there is a charge transfer from Au to MoS_2 , which makes MoS_2 an n-type semiconductor. However, electron transfers from graphene do not correspond to shifts of the Dirac point relative to the Fermi energy, except for the Gr/Au case, in agreement with past reports [34,66]. Thus, charge transfers between graphene and Au and MoS_2 do not necessarily correspond to Dirac point shifts.

The work function for the isolated MoS_2 is larger than the one for the isolated graphene, which is not surprising since $MoS_2(1L)$ is a semiconductor and graphene is a semimetal. Moreover qualitatively, the higher the work function the lower the electrical conductivity. The $MoS_2(1L-2L)$ adsorption on Au decreases the $MoS_2(1L)$ bandgap and its work function value relative to the isolated $MoS_2(1L)$, indicating an improved conductivity for the $MoS_2(1L-2L)/Au$ heterointerfaces. The $MoS_2(1L)/Gr/Au$ has the highest work function from all heterostructures and heterointerfaces in this work. This indicates that the presence of graphene between $MoS_2(1L)/Au$ interface changes the conductivity, such that it becomes useful for photoconductive properties (see Fig. 4) and for devising range of optoelectronic devices.

3.2. Expanding correlations with experimental results

We further expand on correlating the above calculations with experimental findings, and discuss the results related to the work function, the photoconductivity, and the lattice vibrational and optical properties. Fig. 4 shows the SEM images (panels a and b), the optical image (panel c) and the AFM topography (panel d) identifying various surfaces and heterointerfaces and unambiguously visualizes layer

Table 2 Charge transfers per atom relative in units of e with the corresponding error in these calculations and the work function $\Phi = E_{vaccum} - E_{Fermi}$. $\Phi^{MoS_2(1L)} = 5.585\,eV$ and $\Phi^{Gr} = 4.257eV$.

System	q (e)		$\Phi(eV)$			
	Mo	Au	S	С	Error	
MoS ₂ (1L)/Au	-1.194	-3.8×10^{-3}	0.606		10^{-6}	4.930
MoS ₂ (2L)/Au	-1.212	-3.4×10^{-3}	0.610		10^{-6}	4.951
Gr/Au		3.8×10^{-4}		-5.5×10^{-4}	10^{-5}	5.035
MoS ₂ (1L)/Gr/ Au	-1.190	$9.9{ imes}10^{-4}$	0.598	-3.1×10^{-3}	10^{-6}	5.122
Gr/MoS ₂ (1L)	-1.082		0.542	-6.8×10^{-4}	10^{-6}	4.542
Gr/MoS ₂ (1L)/ Gr	-1.064		0.536	-1.2×10^{-3}	10^{-5}	4.447

numbers through contrast for both graphene and MoS₂, as well as MoS₂/ Gr heterostructures. Here, we measured electronic and optical surface properties to probe buried interfaces for MoS2 on Au and MoS2 on graphene. The AFM topography was measured in combination with KPFM obtaining contact potential difference (CPD) showing regions with dark (MoS₂) and bright (graphene or gold) contrast levels. The average CPD was determined through measuring the distribution over nanoregions (Fig. 4f). The work function was calculated using the following eV_{CPD} = $\Phi_{tip} - \Phi_{sample}$, where V_{CPD} in volts, Φ_{tip} is tip work function calibrated with HOPG, Φ_{sample} is of samples and e the electron charge. These values are summarized and plotted in Fig. 4h along with computational values, which are in reasonable agreement with experiment. The tunable work function of MoS₂ (1L and 2L)/Au (111) was calculated to be 4.80 eV and 4.772 eV. The work function of the MoS₂/Gr heterostructure decreased depending upon the number of graphene layers ranged between 40 and 70 meV confirming charge transfer from graphene to MoS₂ at 2D-MoS₂/ graphene heterostructures. Partial change of work function values is attributed to the interface dipole between graphene and MoS2 and the electron density redistribution. Fig. 4g shows conductive AFM (C-AFM) measuring local photo-conductive mapping under laser illumination. The contrast is due to photocurrent modulation of local electric field at the barrier interface, wherein the concentration of charged carriers is varied due to the injection of electrons upon laser illumination. These findings manifested in optimal electronic coupling of dissimilar 2D layers layered materials for light energy harvesting [71].

The lattice vibration properties were also probed using confocal Raman spectroscopy [72,73]. Recall that the space group of a single layer MoS_2 is $P6_3/mmc$ (point group D_{3h}). Consequently, systems with even numbers of layers belong to the space group P3m1 (with inversion symmetry) and systems with odd numbers of layers to the P6₃/mmc space group (without inversion symmetry) [74]. The first- and secondorder Raman spectra (Fig. 5a) highlight signatures associated with planar MoS2 flakes and mono-/bilayer graphene layers, both on Au, and MoS₂ heterostructured interface with the underlying graphene layer. Briefly, the prominent vibrational bands associated with MoS2 include the in-plane $E'(E_{2g}^1$ for bulk) mode at 384.0 cm⁻¹ (383.8) and out-ofplane A_{1}^{\prime} (A_{1g} for bulk) mode at 403.4 cm $^{-1}$ (404.5), with frequency difference $\Delta f = 19.5 \text{ cm}^{-1}$ for mono- (1L) and 20.8 cm⁻¹ for bilayer (2L) consistent with the most of the literature values [4,35]. The spectra in Fig. 5a (middle panel) are related to graphene and interfaces showing a characteristic G band at 1580 cm⁻¹ associated with the in-plane tangential mode. The disorder-activated D band at about 1340 cm⁻¹ was almost absent. The overtone 2D peak $\sim 2670~{\rm cm}^{-1}$ (Fig. 5a, last panel) exhibits frequencies and line shapes matching the characteristic mono or bilayer graphene [3,35]. While the in-plane vibration provides information about in-plane strain, out-of-plane mode provides evidence on the quality of the interfacial contacts. Notably, compared to the MoS₂ (1L-2L)/Au, the E and A_1 mode was red shifted by 1.0 cm⁻¹ and blue shifted by 1.6–2.0 $\mbox{cm}^{-1},$ respectively. In the case of the \mbox{MoS}_2/\mbox{Gr} heterostructure, the vdWH contact is also characterized by a shift of 12-13 cm⁻¹ in the graphene 2D peak. These result from the interlayer interactions with underlying graphene indicates doping of MoS2 monolayer. However, the position of the G band was almost invariant within the uncertainty of the Raman instrumental resolution (less than 1 cm⁻¹).

The optical properties were studied by UV–Visible absorption (Fig. 5b) and photoluminescence (PL) emission (Fig. 5c) spectroscopy. The absorption spectrum yields a reliable measurement of the bandgap either in configuration space or in light scattering momentum space. An obvious broad peak located at ~ 230 nm (and 268 nm) is related to graphene, which differs from larger flakes of 2D-MoS₂ that shows peaks at ~ 620 nm and ~ 668 nm (1.856 eV) ascribed to B and A neutral excitonic peaks, respectively, arising from the K point BZ [4,14,35,69,70]. The $\pi\!\rightarrow\!\pi^*$ transitions in the absorbance data are detected at ~ 250 nm, which is equivalent to about 4.6 eV. The strongest luminescence peak at 450 nm (2.76 eV) is due to direct transitions from

deep valence to conduction band, which shifts with excitation wavelength. The room temperature PL spectra also shows a neutral exciton (A) peak at 1.885 eV, for MoS₂(1L)/Au. This finding is in contrast with the reported observation of quenching of PL signal, which we attributed to conformal contact of MoS₂ with Au [10,75,76]. On the other hand, exciton A peak intensity becomes stronger two to four times on graphene layers than those when placed on Au. The red shift in A peak transition energy by 43 meV is observed for MoS₂(1L)/Gr(1L) heterostructures (Fig. 5c). The crystalline flakes comprised in these heterostructures are randomly misoriented and therefore it is likely the interaction between MoS₂, and graphene is weak. The observed shifts and the enhanced PL signal arise due to the interaction with graphene 'nanospacer' resulting in direct changes in the MoS_2 electronic structure as observed through calculations. Furthermore, the spectral shape of the exciton A is modified such that the emergence of the charged exciton (or trion) peak (A⁻) is observed peaking at 1.835 eV for MoS₂(1L)/Gr heterostructures, yielding trion binding energy of 30 meV, slightly higher than those for MoS₂ (ca. 20 meV) and is suggestive of robust excitons at room temperature. These can be exploited for exciton-photonics technologies, such as quantum sensing and light-energy harvesting. An obvious exciton splitting is attributed to built-in electric field at the MoS₂/Gr interface regardless of the number of graphene layers.

Our experimental results directly and/or indirectly support the optical and electronic properties inferred from calculated band structure, the work function, and the optical properties. The PL spectra can be used to determine changes in the MoS2 bandgaps. This is in a similar fashion as used by Weber and Alonso for determining bandgaps from PL spectra on Si-Ge alloys [77]. Fig. 5c shows that the addition of a second MoS₂ monolayer on top of MoS₂/Au decreases the bandgap, in agreement with our calculations. This is due to the change of the monolayer MoS₂ (1L) bandgap from direct to indirect in the bilayer MoS2 (2L). However, the change in the absorbance is a better approach for determining bandgap changes relative to using the PL spectra. The absorbance data shows that the absorbance peak for MoS₂(1L)/Au is observed at higher wavelengths (smaller eV) than the one from the $MoS_2/Gr/Au$. This means that the MoS₂ bandgap is less in units of eV for the MoS₂(1L)/Au relative to MoS₂(1L)/Gr/Au, in agreement with our calculations. However, the PL spectra showed otherwise albeit marginally.

4. Conclusions

In summary, we performed DFT calculations in MoS₂ and graphene heterointerfaces placed on Au and their heterostructures to unravel the electronic band structure and density of states per atom energy and their work function, as well as their optical properties. We also complemented these calculations with experimental findings, specifically correlated with surface work function and optical photoluminescence bands, highlighting the interaction of the MoS2 with the Au substrate and graphene. The frequency-dependent dielectric function, the refractive index, and the reflectivity were calculated for light polarization parallel and perpendicular to the plane of respective top nanolayer in heterointerfaces and heterostructures. The calculated electronic and optical properties were in reasonable agreement with the past computational reports and with our experimental results. The insertion of graphene layer in-between gold and MoS2 (or vice versa) has significant effects on their electronic and optical behavior despite the weak interlayer interaction. Consequently, interfacing MoS2 with graphene signifies engineered manipulation of physical properties thereby paving the way for their applications in diverse technologies from semiconductors to light energy harvesting and electrocatalysis.

CRediT authorship contribution statement

Sanju Gupta: Conceptualization, Methodology, Data curation, Supervision, Validation, Writing – review & editing. Panagiota Pimenidou: Writing – review & editing. Miguel Garcia: Validation, Writing –

review & editing. **Shivanshi Das:** Validation, Writing – review & editing. **Nicholas Dimakis:** Conceptualization, Methodology, Supervision, Validation, Writing – review & editing.

Declaration of Competing Interest

The authors declare that they have no known competing financial interests or personal relationships that could have appeared to influence the work reported in this paper.

Data availability

Data will be made available on request.

Acknowledgements

The author S.G. acknowledges Dr. S. Khondaker and Mr. A. Johnston for providing facilities and acquisition of some experimental data, respectively, while working at the University of Central Florida. The authors also acknowledge the Texas Advanced Computing Center (TACC) at The University of Texas at Austin for providing High-Performance Computing (HPC) resources that have contributed to the research results reported within this paper.

Data Availability

The raw and processed data that support the findings of this study are available from the corresponding author upon reasonable request.

Appendix A. Supplementary material

Supplementary data to this article can be found online at https://doi. org/10.1016/j.apsusc.2023.156948.

References

- [1] K.S. Novoselov, V.I. Fal'ko, L. Colombo, P.R. Gellert, M.G. Schwab, K. Kim, A roadmap for graphene, Nature 490 (2012) 192–200.
- [2] A.K. Geim, I.V. Grigorieva, Van der Waals heterostructures, Nature 499 (2013) 419–425.
- [3] S. Gupta, E. Heintzman, J. Jasinski, Multiphonon Raman spectroscopy properties and Raman mapping of 2D van der Waals solids: graphene and beyond, J. Raman Spectrosc. 46 (2015) 217–230.
- [4] K.F. Mak, C. Lee, J. Hone, J. Shan, T.F. Heinz, Atomically Thin MoS₂: A New Direct-Gap Semiconductor, Phys. Rev. Lett. 105 (2010) 136805–1136804.
- [5] Q.H. Wang, K. Kalantar-Zadeh, A. Kis, J.N. Coleman, M.S. Strano, Electronics and optoelectronics of two-dimensional transition metal dichalcogenides, Nat. Nanotechnol. 7 (2012) 699–712.
- [6] N. Thomas, S. Mathew, K.M. Nair, K. O'Dowd, P. Forouzandeh, A. Goswami, G. McGranaghan, S.C. Pillai, 2D MoS2: structure, mechanisms, and photocatalytic applications, Mater. Today Sustain. 13 (2021), 100073.
- [7] D. Jariwala, V.K. Sangwan, L.J. Lauhon, T.J. Marks, M.C. Hersam, Emerging Device Applications for Semiconducting Two-Dimensional Transition Metal Dichalcogenides, ACS Nano 8 (2014) 1102–1120.
- [8] L. Wang, I. Meric, P.Y. Huang, Q. Gao, Y. Gao, H. Tran, T. Taniguchi, K. Watanabe, L.M. Campos, D.A. Muller, J. Guo, P. Kim, J. Hone, K.L. Shepard, C.R. Dean, One-Dimensional Electrical Contact to a Two-Dimensional Material, Science 342 (2013) 614–617.
- [9] F.H.L. Koppens, T. Mueller, P. Avouris, A.C. Ferrari, M.S. Vitiello, M. Polini, Photodetectors based on graphene, other two-dimensional materials and hybrid systems, Nat. Nanotechnol 9 (2014) 780–793.
- [10] K. Jo, P. Kumar, J. Orr, S.B. Anantharaman, J. Miao, M.J. Motala, A. Bandyopadhyay, K. Kisslinger, C. Muratore, V.B. Shenoy, E.A. Stach, N. R. Glavin, D. Jariwala, Direct Optoelectronic Imaging of 2D Semiconductor–3D Metal Buried Interfaces. ACS Nano 15 (2021) 5618–5630.
- [11] Y. Cao, V. Fatemi, S. Fang, K. Watanabe, T. Taniguchi, E. Kaxiras, P. Jarillo-Herrero, Unconventional superconductivity in magic-angle graphene superlattices, Nature 556 (2018) 43–50.
- [12] L. Britnell, R.V. Gorbachev, R. Jalil, B.D. Belle, F. Schedin, A. Mishchenko, T. Georgiou, M.I. Katsnelson, L. Eaves, S.V. Morozov, N.M.R. Peres, J. Leist, A. K. Geim, K.S. Novoselov, L.A. Ponomarenko, Field-Effect Tunneling Transistor Based on Vertical Graphene Heterostructures. Science 335 (2012) 947–950.
- [13] Y. Gong, J. Lin, X. Wang, G. Shi, S. Lei, Z. Lin, X. Zou, G. Ye, R. Vajtai, B.I. Yakobson, H. Terrones, M. Terrones, Beng K. Tay, J. Lou, S.T. Pantelides, Z. Liu, W.

- Zhou, P.M. Ajayan, Vertical and in-plane heterostructures from WS_2/MoS_2 monolayers, Nat. Mater., 13 (2014) 1135-1142.
- [14] S. Gupta, T. Robinson, N. Dimakis, Electrochemically Desulfurized Molybdenum Disulfide (MoS₂) and Reduced Graphene Oxide Aerogel Composites as Efficient Electrocatalysts for Hydrogen Evolution, J. Nanosci. Nanotechnol. 20 (2020) 6191–6214
- [15] X. Hong, J. Kim, S.-F. Shi, Y. Zhang, C. Jin, Y. Sun, S. Tongay, J. Wu, Y. Zhang, F. Wang, Ultrafast charge transfer in atomically thin MoS₂/WS₂ heterostructures, Nat. Nanotechnol 9 (2014) 682–686.
- [16] M. Yankowitz, J. Xue, D. Cormode, J.D. Sanchez-Yamagishi, K. Watanabe, T. Taniguchi, P. Jarillo-Herrero, P. Jacquod, B.J. LeRoy, Emergence of superlattice Dirac points in graphene on hexagonal boron nitride, Nature Physics 8 (2012) 382–386
- [17] C.R. Dean, L. Wang, P. Maher, C. Forsythe, F. Ghahari, Y. Gao, J. Katoch, M. Ishigami, P. Moon, M. Koshino, T. Taniguchi, K. Watanabe, K.L. Shepard, J. Hone, P. Kim, Hofstadter's butterfly and the fractal quantum Hall effect in moiré superlattices, Nature 497 (2013) 598–602.
- [18] K. Roy, M. Padmanabhan, S. Goswami, T.P. Sai, G. Ramalingam, S. Raghavan, A. Ghosh, Graphene–MoS₂ hybrid structures for multifunctional photoresponsive memory devices, Nat. Nanotechnol 8 (2013) 826–830.
- [19] O. Lopez-Sanchez, D. Lembke, M. Kayci, A. Radenovic, A. Kis, Ultrasensitive photodetectors based on monolayer MoS₂, Nat. Nanotechnol 8 (2013) 497–501.
- [20] S. Gao, Z. Wang, H. Wang, F. Meng, P. Wang, S. Chen, Y. Zeng, J. Zhao, H. Hu, R. Cao, Z. Xu, Z. Guo, H. Zhang, Graphene/MoS₂/Graphene Vertical Heterostructure-Based Broadband Photodetector with High Performance, Adv. Mater. Interfaces 8 (2021) 2001730.
- [21] T. Georgiou, R. Jalil, B.D. Belle, L. Britnell, R.V. Gorbachev, S.V. Morozov, Y.-J. Kim, A. Gholinia, S.J. Haigh, O. Makarovsky, L. Eaves, L.A. Ponomarenko, A. K. Geim, K.S. Novoselov, A. Mishchenko, Vertical field-effect transistor based on graphene–WS₂ heterostructures for flexible and transparent electronics, Nat. Nanotechnol 8 (2013) 100–103.
- [22] M. Massicotte, P. Schmidt, F. Vialla, K.G. Schädler, A. Reserbat-Plantey, K. Watanabe, T. Taniguchi, K.J. Tielrooij, F.H.L. Koppens, Picosecond photoresponse in van der Waals heterostructures, Nat. Nanotechnol 11 (2016) 42–46.
- [23] F. Withers, O. Del Pozo-Zamudio, A. Mishchenko, A.P. Rooney, A. Gholinia, K. Watanabe, T. Taniguchi, S.J. Haigh, A.K. Geim, A.I. Tartakovskii, K. S. Novoselov, Light-emitting diodes by band-structure engineering in van der Waals heterostructures, Nat. Mater. 14 (2015) 301–306.
- [24] H. Coy Diaz, J. Avila, C. Chen, R. Addou, M.C. Asensio, M. Batzill, Direct Observation of Interlayer Hybridization and Dirac Relativistic Carriers in Graphene/MoS₂ van der Waals Heterostructures, Nano Lett., 15 (2015) 1135-1140.
- [25] G.W. Shim, K. Yoo, S.-B. Seo, J. Shin, D.Y. Jung, I.-S. Kang, C.W. Ahn, B.J. Cho, S. Y. Choi, Large-Area Single-Layer MoSe₂ and Its van der Waals Heterostructures, ACS Nano 8 (2014) 6655–6662.
- [26] S. Subramanian, K. Xu, Y. Wang, S. Moser, N.A. Simonson, D. Deng, V.H. Crespi, S. K. Fullerton-Shirey, J.A. Robinson, Tuning transport across MoS₂/graphene interfaces via as-grown lateral heterostructures, npj 2D Mater, Appl. 4 (2020) 9.
- [27] H.V. Phuc, N.N. Hieu, B.D. Hoi, L.T.T. Phuong, C.V. Nguyen, First principle study on the electronic properties and Schottky contact of graphene adsorbed on MoS2 monolayer under applied out-plane strain, Surf. Sci. 668 (2018) 23–28.
- [28] B. Qiu, X. Zhao, G. Hu, W. Yue, J. Ren, X. Yuan, Optical Properties of Graphene/ MoS2 Heterostructure: First Principles Calculations, Nanomaterials 8 (2018) 962.
- [29] P. Hohenberg, W. Kohn, Inhomogeneous Electron Gas, Phys. Rev. 136 (1964) B864–B871.
- [30] W. Kohn, L.J. Sham, Self-Consistent Equations Including Exchange and Correlation Effects, Phys. Rev. 140 (1965) A1133–A1138.
- [31] N. Dimakis, S. Gupta, R. Wazzen, M.I. Bhatti, Dry and Hydrated Defective Molybdenum Disulfide/Graphene Bilayer Heterojunction Under Strain for Hydrogen Evolution from Water Splitting: A First-principle Study, Comput. Mat. Sci. 205 (2022), 111234.
- [32] S. Singh, C. Espejo, A.H. Romero, First-principles investigation of graphene/MoS₂ bilayer heterostructures using Tkatchenko-Sche er van der Waals method, Phys. Rev. B 98 (2018) 155309–155310.
- [33] A. Bruix, J.A. Miwa, N. Hauptmann, D. Wegner, S. Ulstrup, S.S. Grønborg, C. E. Sanders, M. Dendzik, A. Grubišić Čabo, M. Bianchi, J.V. Lauritsen, A. A. Khajetoorians, B. Hammer, P. Hofmann, Single-layer MoS₂ on Au(111): Band gap renormalization and substrate interaction, Phys. Rev. B 93 (2016), 165422.
- [34] M. Yortanlı, E. Mete, Common surface structures of graphene and Au(111): The effect of rotational angle on adsorption and electronic properties, J. Chem. Phys. 151 (2019), 214701.
- [35] S. Gupta, A. Johnston, S. Khondaker, Optoelectronic Properties of MoS2/Graphene Heterostructures Prepared by Dry Transfer for Light-Induced Energy Applications, J. Electron. Mater. 51 (2022) 4257–4269.
- [36] G. Kresse, J. Hafner, Ab initio molecular dynamics for liquid metals, Phys. Rev. B 47 (1993) 558(R)–561(R).
- [37] G. Kresse, J. Hafner, Ab initio molecular-dynamics simulation of the liquid-metal–amorphous-semiconductor transition in germanium, Phys. Rev. B 49 (1994) 14251–14269.
- [38] G. Kresse, J. Furthmüller, Efficiency of ab-initio total energy calculations for metals and semiconductors using a plane-wave basis set, Comput. Mater. Sci. 6 (1996) 15–50.
- [39] G. Kresse, J. Furthmüller, Efficient iterative schemes for ab initio total-energy calculations using a plane-wave basis set, Phys. Rev. B 54 (1996) 11169–11186.
- [40] G. Kresse, D. Joubert, From ultrasoft pseudopotentials to the projector augmentedwave method, Phys. Rev. B 59 (1999) 1758–1775.

- [41] P.E. Blöchl, Projector augmented-wave method, Phys. Rev. B 50 (1994) 17953–17979.
- [42] J.P. Perdew, K. Burke, M. Ernzerhof, Generalized gradient approximation made simple, Phys. Rev. Lett. 77 (1996) 3865.
- [43] S. Grimme, J. Antony, S. Ehrlich, H. Krieg, A consistent and accurate ab initio parametrization of density functional dispersion correction (DFT-D) for the 94 elements H-Pu, J. Chem. Phys. 132 (2010) 154104–154119.
- [44] R. Bader, Atoms in Molecules: A Quantum Theory, Oxford Univ. Press, in, Oxford, 1990
- [45] W. Tang, E. Sanville, G. Henkelman, A grid-based Bader analysis algorithm without lattice bias, J. Phys. Condens. Matter 21 (2009), 084204.
- [46] E. Sanville, S.D. Kenny, R. Smith, G. Henkelman, Improved grid-based algorithm for Bader charge allocation, J. Comput. Chem. 28 (2007) 899–908.
- [47] G. Henkelman, A. Arnaldsson, H. Jónsson, A fast and robust algorithm for Bader decomposition of charge density, Comput. Mater. Sci. 36 (2006) 354–360.
- [48] M. Yu, D.R. Trinkle, Accurate and efficient algorithm for Bader charge integration, J. Chem. Phys. 134 (2011), 064111.
- [49] A. Delin, P. Ravindran, O. Eriksson, J.M. Wills, Full-potential optical calculations of lead chalcogenides, Int. J. Quantum Chem. 69 (1998) 349–358.
- [50] P. Rivera, W. Yao, X. Xu, Optical Properties of TMD Heterostructures, in: P. Avouris, T. Low, T.F. Heinz (Eds.), 2D Materials: Properties and Devices, Cambridge University Press, Cambridge, 2017, pp. 310–328.
- [51] A.H. Reshak, S. Auluck, Calculated optical properties of 2H-MoS₂ intercalated with lithium, Phys. Rev. B 68 (2003), 125101.
- [52] S.L. Adler, Quantum Theory of the Dielectric Constant in Real Solids, Phys. Rev. 126 (1962) 413–420.
- [53] H. Ehrenreich, M.H. Cohen, Self-Consistent Field Approach to the Many-Electron Problem, Phys. Rev. 115 (1959) 786–790.
- [54] P. Rani, G.S. Dubey, V.K. Jindal, DFT study of optical properties of pure and doped graphene, Physica E Low Dimens. Syst. Nanostruct. 62 (2014) 28–35.
- [55] A.G. Marinopoulos, L. Reining, A. Rubio, V. Olevano, Ab initio study of the optical absorption and wave-vector-dependent dielectric response of graphite, Phys. Rev. B 69 (2004), 245419.
- [56] W. Orellana, J.D. Correa, Noncovalent functionalization of carbon nanotubes and graphene with tetraphenylporphyrins: stability and optical properties from ab initio calculations, J. Mater. Sci. 50 (2015) 898–905.
- [57] J. Pešić, J. Vujin, T. Tomašević-Ilić, M. Spasenović, R. Gajić, DFT study of optical properties of MoS₂ and WS₂ compared to spectroscopic results on liquid phase exfoliated nanoflakes, Opt. Quantum Electron. 50 (2018) 291.
- [58] B. Rajbanshi, S. Sarkar, P. Sarkar, The electronic and optical properties of MoS₂ (1-x)Se_{2x} and MoS_{2(1-x)}Te_{2x} monolayers, Phys. Chem. Chem. Phys. 17 (2015) 26166–26174.
- [59] O.V. Sedelnikova, L.G. Bulusheva, A.V. Okotrub, Ab initio study of dielectric response of rippled graphene, J. Chem. Phys. 134 (2011), 244707.
- [60] J.-Q. Hu, X.-H. Shi, S.-Q. Wu, K.-M. Ho, Z.-Z. Zhu, Dependence of Electronic and Optical Properties of MoS₂ Multilayers on the Interlayer Coupling and Van Hove Singularity, Nanoscale Res. Lett. 14 (2019) 288.

- [61] A. Dashora, U. Ahuja, K. Venugopalan, Electronic and optical properties of MoS₂ (0001) thin films: Feasibility for solar cells, Comput. Mater. Sci. 69 (2013) 216–221.
- [62] A. Mashmool, P. Saeidi, S. Yalameha, Z. Nourbakhsh, First principles calculations of structural, electronic and optical properties MoX₂ (X = S, Se) metal dichalcogenides and their nano-layers, J. Magn. Magn. Mater. 503 (2020), 166572.
- [63] M. Kan, J.Y. Wang, X.W. Li, S.H. Zhang, Y.W. Li, Y. Kawazoe, Q. Sun, P. Jena, Structures and Phase Transition of a MoS₂ Monolayer, J. Phys. Chem. C 118 (2014) 1515–1522.
- [64] F. Lahourpour, A. Boochani, S.S. Parhizgar, S.M. Elahi, Structural, electronic and optical properties of graphene-like nano-layers MoX₂(X:S, Se, Te): DFT study, J. Theor. Appl. Phys. 13 (2019) 191–201.
- [65] X. Li, H. Zhu, Two-dimensional MoS₂: Properties, preparation, and applications, J. Materiomics 1 (2015) 33–44.
- [66] P.A. Khomyakov, G. Giovannetti, P.C. Rusu, G. Brocks, J. van den Brink, P.J. Kelly, First-principles study of the interaction and charge transfer between graphene and metals, Phys. Rev. B 79 (2009), 195425.
- [67] Z.-Y. Zhao, Q.-L. Liu, Study of the layer-dependent properties of MoS₂ nanosheets with different crystal structures by DFT calculations, Catal. Sci. Technol. 8 (2018) 1867–1879.
- [68] P.B. Johnson, R.W. Christy, Optical Constants of the Noble Metals, Phys. Rev. B 6 (1972) 4370–4379.
- [69] S. Gupta, A. Johnston, S. Khondaker, Correlated KPFM and TERS imaging to elucidate defect-induced inhomogeneities in oxygen plasma treated 2D MoS₂ nanosheets, J. Appl. Phys. 131 (2022), 164303.
- [70] S. Gupta, A. Johnston, S. Khondaker, Surface and Physical Properties Modifications of Electron Beam-Irradiated Monolayer MoS₂-Au Heterointerface at Nanoscale, J. Electron. Mater. (2022).
- [71] S.M. Sze, M.K. Lee, Semiconductor Devices, John Willey & Sons Inc, New Jersey, 2007
- [72] J.L. Verble, T.J. Wieting, Lattice Mode Degeneracy in MoS₂ and Other Layer Compounds, Phys. Rev. Lett. 25 (1970) 362–365.
- [73] J.A. Wilson, A.D. Yoffe, The transition metal dichalcogenides discussion and interpretation of the observed optical, electrical and structural properties, Adv. Phys. 18 (1969) 193–335.
- [74] A. Molina-Sánchez, L. Wirtz, Phonons in single-layer and few-layer MoS₂ and WS₂, Phys. Rev. B 84 (2011), 155413.
- [75] A. Splendiani, L. Sun, Y. Zhang, T. Li, J. Kim, C.-Y. Chim, G. Galli, F. Wang, Emerging Photoluminescence in Monolayer MoS₂, Nano Lett. 10 (2010) 1271–1275.
- [76] M. Buscema, G.A. Steele, H.S.J. van der Zant, A. Castellanos-Gomez, The effect of the substrate on the Raman and photoluminescence emission of single-layer MoS₂, Nano Res. 7 (2014) 561–571.
- [77] J. Weber, M.I. Alonso, Near-band-gap photoluminescence of Si-Ge alloys, Phys. Rev. B 40 (1989) 5683–5693.